

See discussions, stats, and author profiles for this publication at: <https://www.researchgate.net/publication/7378067>

Modeling solvent effects on electron spin resonance hyperfine couplings by frozen-density embedding

ARTICLE *in* THE JOURNAL OF CHEMICAL PHYSICS · OCTOBER 2005

Impact Factor: 2.95 · DOI: 10.1063/1.2033749 · Source: PubMed

CITATIONS

49

READS

55

5 AUTHORS, INCLUDING:



Paola Belanzoni

Università degli Studi di Perugia

55 PUBLICATIONS 702 CITATIONS

SEE PROFILE



Tomasz A Wesolowski

University of Geneva

106 PUBLICATIONS 3,148 CITATIONS

SEE PROFILE



Evert Jan Baerends

VU University Amsterdam

481 PUBLICATIONS 39,255 CITATIONS

SEE PROFILE

Modeling solvent effects on electron-spin-resonance hyperfine couplings by frozen-density embedding

Johannes Neugebauer^{a)} and Manuel J. Louwerse^{b)}

Theoretical Chemistry, Vrije Universiteit Amsterdam, De Boelelaan 1083, 1081 HV Amsterdam, The Netherlands

Paola Belanzoni^{c)}

Dipartimento di Chimica, Università di Perugia, Via Elce di Sotto 8, 06123 Perugia, Italy

Tomasz A. Wesolowski^{d)}

Department of Physical Chemistry, University of Geneva, 30 quai Ernest-Ansermet, CH-1211 Geneva 4, Switzerland

Evert Jan Baerends^{e)}

Theoretical Chemistry, Vrije Universiteit Amsterdam, De Boelelaan 1083, 1081 HV Amsterdam, The Netherlands

(Received 14 June 2005; accepted 19 July 2005; published online 16 September 2005)

In this study, we investigate the performance of the frozen-density embedding scheme within density-functional theory [J. Phys. Chem. **97**, 8050 (1993)] to model the solvent effects on the electron-spin-resonance hyperfine coupling constants (hfcc's) of the H_2NO molecule. The hfcc's for this molecule depend critically on the out-of-plane bending angle of the NO bond from the molecular plane. Therefore, solvent effects can have an influence on both the electronic structure for a given configuration of solute and solvent molecules and on the probability for different solute (plus solvent) structures compared to the gas phase. For an accurate modeling of dynamic effects in solution, we employ the Car-Parrinello molecular-dynamics (CPMD) approach. A *first-principles*-based Monte Carlo scheme is used for the gas-phase simulation, in order to avoid problems in the thermal equilibration for this small molecule. Calculations of small H_2NO -water clusters show that microsolvation effects of water molecules due to hydrogen bonding can be reproduced by frozen-density embedding calculations. Even simple sum-of-molecular-densities approaches for the frozen density lead to good results. This allows us to include also bulk solvent effects by performing frozen-density calculations with many explicit water molecules for snapshots from the CPMD simulation. The electronic effect of the solvent at a given structure is reproduced by the frozen-density embedding. Dynamic structural effects in solution are found to be similar to the gas phase. But the small differences in the average structures still induce significant changes in the computed shifts due to the strong dependence of the hyperfine coupling constants on the out-of-plane bending angle. © 2005 American Institute of Physics. [DOI: 10.1063/1.2033749]

I. INTRODUCTION

Quantum chemical calculations of electron-spin-resonance (ESR) parameters have become a routinely applicable task during the past years (for an excellent overview, see the book by Kaupp *et al.*¹⁾). Particularly density-functional methods are widely used to study g tensors and hyperfine splittings, and their performance has been investigated in recent studies (see, e.g., Refs. 2–4). For many systems, these parameters depend strongly on the environment.

Isotropic hyperfine coupling constants (hfcc's) are very sensitive to solvent effects in two respects. First, they often show a strong dependence on the structure of the molecule, and the solvent may have a great influence on certain struc-

tural parameters. Second, also for a given distribution of structures, solvation can change the values of the hfcc's significantly. Therefore, accurate calculations of these quantities must account for both structural changes between gas phase and solvent as well as for solvent effects at a given structure.⁵

Among the best studied radicals are (organic) π radicals, e.g., nitroxides, semiquinones, or phenoxyls. They have been subject to numerous theoretical investigations, and many aspects of solvent effects on their ESR parameters have been analyzed.^{6–13} One prototype system for the family of nitroxides is the H_2NO radical, which shows a strong dependence of the hfcc's on the out-of-plane bending angle θ of the NO group from the H–N–H plane. The singly occupied molecular orbital (SOMO) in this case is a π^* -type orbital perpendicular to the molecular plane. An isosurface plot of the SOMO is shown in Fig. 1. For $\theta=0$, the direct contribution of the SOMO to the hyperfine coupling constants vanishes for all atoms, since there is no contribution of s -type atomic

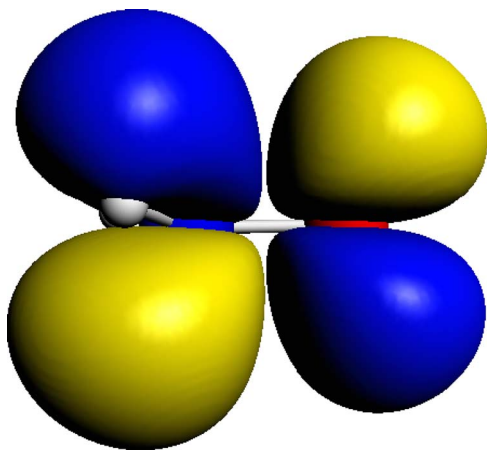
^{a)}Electronic mail: jneugeb@chem.vu.nl

^{b)}Electronic mail: louwerse@chem.vu.nl

^{c)}Electronic mail: paola@thch.unipg.it

^{d)}Electronic mail: tomasz.wesolowski@chiphys.unige.ch

^{e)}Electronic mail: baerends@chem.vu.nl

FIG. 1. Isosurface plot of the H₂NO SOMO.

orbitals to the SOMO for symmetry reasons. It is an ideal example molecule since many experimental studies in gas phase,¹⁴ argon matrix,¹⁵ water,¹⁶ and methanol¹⁷ have been carried out. Earlier theoretical studies concerning the solvent effects on this molecule employed mixed classical and quantum chemical approaches. Takase and Kikuchi used snapshots generated from classical Monte Carlo simulations, in which only the angle θ was freely varied. Hyperfine coupling constants were obtained for these structures by restricted open-shell Hartree-Fock- (ROHF) type calculations, in which a classical point-charge model was used to include the effect of the solvent.¹⁸ In this way, only electrostatic effects of the solvent are covered. Later, Barone *et al.* studied environmental effects by combining static hybrid density-functional theory calculations of the hyperfine coupling constants with classical polarizable continuum solvent models.¹⁹ Although the dependence of the hyperfine coupling constants on the angle θ was investigated in that study, the vibrational effect on the average ESR parameters is not explicitly given. It was, however, mentioned there that in a related study on H₂NO *in vacuo*¹⁹ the vibrational averaging effect for the out-of-plane vibration on this radical was small.

Studies on other nitroxide radicals showed that a more sophisticated treatment might be necessary in some cases, where dynamical fluctuations of hydrogen-bonded systems have to be described.¹³ A Car-Parrinello molecular-dynamics (CPMD) approach was used in Ref. 13 to sample the space of accessible configurations for the solvated system, since earlier studies¹¹ showed that the angular distribution around the NO group might not be reliably reproduced by studies based on classical force fields as presented in Ref. 12. For the calculation of hyperfine coupling constants, different methods combining explicit (quantum) water molecules, classical water models, and continuum models were applied for 100 snapshots of the CPMD simulation to simulate bulk solvent effects in Ref. 13.

In this study, we are going to apply a sequential scheme of *first-principles*-based CPMD or Monte Carlo simulations for the structure generation with the frozen-density embedding scheme²⁰ to model solvent effects on the hyperfine coupling constants. It has already been shown that specific solvent-solute interactions (e.g., hydrogen bonding) and bulk

solvent effects on absorption spectra can be modeled by this quantum mechanics (QM)/QM-embedding approach.^{21–23} Here, we are going to assess its reliability in the calculations of hyperfine coupling constants of solvated molecules.

This work goes beyond earlier studies in many respects and combines the advantages of several solvent models: (i) dynamical effects in both gas phase and solution are considered on the basis of first-principles electronic structure methods without restriction of the averaging process to certain degrees of freedom, (ii) problems in the gas-phase simulation due to the weak coupling between different vibrational modes were circumvented by a Monte Carlo scheme, (iii) both short-range electronic (or microsolvation) and bulk solvent effects can be studied by this efficient explicit solvent model, (iv) frozen-density embedding includes not only electrostatic effects but also nonelectrostatic effects (exchange-correlation contributions and nonadditive kinetic-energy effects), and (v) no empirical information enters the calculation of the hyperfine coupling constants in the presence of the solute—apart from the usual parametrization in the density functionals. A direct comparison to experimental data obtained in different media is therefore possible by this approach, which considers both the electronic and the structural changes in the solute upon solvation.

II. COMPUTATIONAL DETAILS

We use the orbital-free embedding formalism²⁰ as employed in Ref. 22 to model solvent effects on the spectroscopic properties in solution. In this formalism, the electron density of the embedded subsystem (ρ_I) in a given microscopic environment, which is represented by means of the frozen electron density (ρ_{II}) and a set of nuclear charges ($Z_{A_{II}}$) at the corresponding positions ($\mathbf{R}_{A_{II}}$), is derived from Kohn-Sham-type one-electron equations. The effective Kohn-Sham (KS) potential in these equations is derived from the requirement that the total density $\rho_{\text{total}} = \rho_I + \rho_{II}$ of the system is obtained, which minimizes the total energy, from an optimization process in which the density of the environment, ρ_{II} , is kept frozen. Assuming that the complementary ρ_I is positive definite and noninteracting v_s representable, KS-type equations can be derived, in which the effect of ρ_{II} is folded into the effective KS potential for the ρ_I system. This effective potential and the corresponding equations are denoted as Kohn-Sham approach with constrained electron density (KSCED). The KSCED effective potential contains the nuclear attraction, electron Coulomb, and exchange-correlation potentials for the isolated system I plus an additional (embedding) component,

$$V_{\text{emb}}^{\text{eff}}[\mathbf{r}, \rho_I, \rho_{II}] = \sum_{A_{II}} -\frac{Z_{A_{II}}}{|\mathbf{r} - \mathbf{R}_{A_{II}}|} + \int \frac{\rho_{II}(\mathbf{r}')}{|\mathbf{r}' - \mathbf{r}|} d\mathbf{r}' + \left. \frac{\delta E_{\text{xc}}[\rho]}{\delta \rho} \right|_{\rho=\rho_I+\rho_{II}} - \left. \frac{\delta E_{\text{xc}}[\rho]}{\delta \rho} \right|_{\rho=\rho_I} + \left. \frac{\delta T_s[\rho]}{\delta \rho} \right|_{\rho=\rho_I+\rho_{II}} - \left. \frac{\delta T_s[\rho]}{\delta \rho} \right|_{\rho=\rho_I}, \quad (1)$$

where we may also write the kinetic part of the potential as

the functional derivative $\delta T_s^{\text{nad}}[\rho_I, \rho_{II}]/\delta \rho_I$ of the nonadditive kinetic-energy functional,

$$T_s^{\text{nad}}[\rho_I, \rho_{II}] = T_s[\rho_I + \rho_{II}] - T_s[\rho_I] - T_s[\rho_{II}]. \quad (2)$$

The functionals $E_{\text{xc}}[\rho]$ and $T_s[\rho]$ are defined in the Kohn-Sham formulation of density-functional theory (DFT).

It is worthwhile to underline that ρ_{II} enters as a given (frozen) function $\rho_{II}(\mathbf{r})$ in Eq. (1). For each choice for this function, one-electron equations for embedded orbitals (KSCED) can be solved. The density ρ_{II} can be obtained from a fully variational treatment of the total system as in the subsystem formulation of density-functional theory by Cortona,²⁴ or it can be subject to additional simplifications to be used in multilevel computer simulations to couple subsystems described at different levels.²⁰

For $T_s[\rho]$ in Eq. (1), we use the gradient-dependent approximation denoted as PW91k in Ref. 22, which is related to the exchange functional of Perdew and Wang²⁵ with a reparametrization by Lembarki and Chermette.²⁶ The accuracy of this approximation has been tested in former studies.^{27,28}

All density-functional calculations, apart from the CPMD simulations, have been performed using the Amsterdam density-functional (ADF) package.^{29,30} We have employed the ZORA-QZ4P basis set from the ADF basis set library, which is of valence quadruple- ζ quality and contains four sets of polarization functions. The Becke-Perdew exchange-correlation functional, dubbed BP86,^{31,32} has been used, which has been shown to yield reliable results for the calculations of ESR hyperfine coupling constants.³ The spin-unrestricted approach has been applied to investigate spin-polarization effects. No frozen-core approximations have been made here. Spin-restricted, spin-orbit-coupled equations within the zero-order regular approximation^{33–35} (ZORA) have been used for the evaluation of the g tensor, which parametrizes the Zeeman interaction. For many systems the spin-orbit coupling is the most important factor for shifting the g -tensor components away from the free-electron value g_e . Its effect on the hyperfine coupling tensor is often quite small. Therefore, the effect of spin polarization on the hyperfine interactions is included in our spin-unrestricted calculations, but not the effect of spin-orbit coupling. The method used here to calculate the g tensor and the hfcc's is described in detail in Refs. 36 and 37.

Structures employed for the investigation of specific interactions between H_2NO and water molecules are fully optimized for the corresponding method and basis set.

To compute the shift in the hyperfine coupling constants, it is necessary to sample the configurational space in gas phase and solution, respectively. For the aqueous solution, CPMD simulations have been carried out with the projector augmented-wave (PAW) package³⁸ using the BLYP functional.^{31,39} The cutoff for the plane-wave basis was 30 Ry (408 eV) and 90 Ry (1225 eV) for the charge density. Using the projector augmented-wave approach rather low plane-wave cutoffs can be used, comparable to Vanderbilt's ultrasoft pseudopotentials, and lower than those necessary with, e.g., Troullier-Martins norm-conserving pseudopotentials.^{38,40} For sampling efficiency reasons, we employed

deuterium isotopes for the hydrogen atoms. We used a fictitious mass for the wave functions of 100 a.u., a time step of 6.5 a.u. (0.157 fs), and a small friction on the wave functions of 0.0002. This has been verified to give good simulations of liquid water. Within the projector augmented-wave technique in the CPMD simulations, a frozen-core approximation was used for the 1s orbitals of oxygen and nitrogen. The simulation was performed with one H_2NO molecule and 32 water molecules in a periodic cubic box of 10.05 Å. A Nosé thermostat with an oscillation frequency of 60 000 a.u. was used to keep the temperature at 300 K. After equilibration for 15 ps with more strongly coupled thermostats, the simulation was prolonged for 12 ps.

For all subsequent frozen-density calculations the frozen density, ρ_{II} in Eq. (1), has been calculated from a sum of molecular densities of solvent molecules obtained within the local-density approximation (LDA) and a TZP basis set. In Ref. 22 it was shown that this approach enormously speeds up the generation of the frozen density without significant loss of accuracy.

For canonical ensemble (constant temperature) gas-phase simulations of such a small molecule, (CP)MD approaches introduce the problem that it is not possible to use conventional thermostating techniques. Tests using a scheme similar to the one used in Ref. 22 for the gas-phase simulation showed that there is no exchange of energy between the different degrees of freedom in the present molecule during the simulation time, so that no proper sampling of the configurational space is achieved. We therefore used a Monte Carlo sampling in internal coordinates, in which ADF-DFT calculations were performed to determine the potential energy of the trial structures. An acceptance ratio of 0.5 was used for the Monte Carlo sampling, and the probabilities of acceptance have been scaled by the factors arising from the Jacobian due to the use of nonlinear coordinates (see the examples in Refs. 41 and 42).

III. STRUCTURAL AND ELECTRONIC EFFECTS OF MICROSOLVATION

From former studies,^{18,43} it is known that there is a strong dependence of the ^1H and ^{14}N hyperfine coupling constants on the out-of-plane bending angle θ of the NO group from the molecular plane. This is due to the fact that the largest contribution to the hfcc is usually the direct contribution of the SOMO, as long as the SOMO does not vanish at the position of the nuclei. The SOMO of dihydronitroxide is essentially the antibonding π^* orbital localized on the nitrogen and the oxygen atoms of the nitroxide moiety, which is perpendicular to the molecular plane (see Fig. 1). The direct contribution from the SOMO thus vanishes for all nuclei if the molecule assumes a planar structure. Deviations from the planarity of the radical center allow the participation of s atomic orbitals to the SOMO, thus increasing the contact spin density considerably.

We calculated the hfcc's for different out-of-plane bending angles, where we optimized all other internal degrees of freedom of the molecule. The results are shown in Fig. 2. Comparison with Ref. 43 shows that our results are in agree-

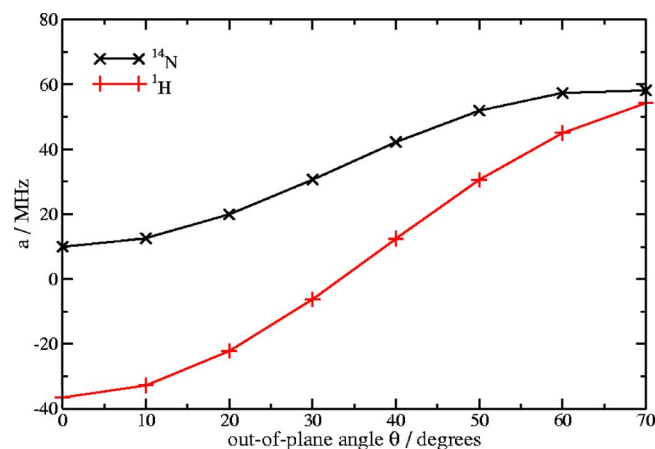


FIG. 2. Dependence of the isotropic hfcc a on the out-of-plane bending angle θ of the NO group from the molecular plane. For each angle θ , all other internal coordinates of the molecule have been optimized (BP86/ZORA-QZ4P).

ment with the curve calculated in that study using the hybrid B3LYP functional.^{44,45} In our case, $a(^1\text{H})$ is -36.5 MHz for the planar structure, becomes zero for $\theta \approx 33^\circ$, and increases to 45.0 MHz for $\theta = 60^\circ$. In Ref. 43, the value for the planar structure is -40.6 MHz, which is a bit lower than in our case. Similar to our case, the hyperfine coupling constant vanishes for $\theta \approx 35^\circ$, and increases to ≈ 42 MHz for $\theta = 60^\circ$. Also for $a(^{14}\text{N})$, we observe similar behavior in both studies. In our case, the value increases from 10.0 MHz for the planar structure to 57.4 MHz for $\theta = 60^\circ$, while the corresponding B3LYP data are 15.1 MHz ($\theta = 0^\circ$) and ≈ 56 MHz ($\theta = 60^\circ$). Both DFT methods seem to underestimate the hyperfine splitting at the equilibrium structure for ^{14}N (but not for ^1H) when compared to UQCISD[T] calculations:⁴³ While BP86 and B3LYP yield 17.8 MHz (BP86; $\theta = 17.6^\circ$) and 21.3 MHz (B3LYP; $\theta = 16.6^\circ$), the UQCISD[T] value of 28.3 MHz ($\theta = 16.9^\circ$) is considerably higher. A similar observation was made for H_2CN ,⁴⁶ which was attributed to an underestimation of spin-polarization effects by DFT methods.

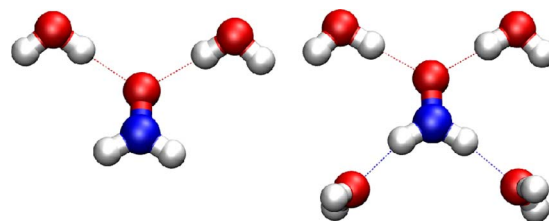


FIG. 3. Optimized structures (BP86/ZORA-QZ4P, no symmetry constraints) of two small H_2NO -water clusters.

In contrast to this, the angular behavior of the hyperfine splittings calculated in Ref. 18 is very different. ROHF calculations have been used in that work, combined with a certain type of singly excited determinants to include spin-polarization effects.^{47,48} The resulting hyperfine coupling constants are approximately -31 MHz for $a(^1\text{H})$ and 34 MHz for $a(^{14}\text{N})$, calculated for the planar structure. The angular dependency for $a(^1\text{H})$ is only in qualitative agreement with the one observed here and in Ref. 43 for smaller angles, and especially for larger angles it is much lower than the DFT results.

In order to investigate the effect of specific electronic interactions of water molecules and the H_2NO radical on the molecular structure and the ESR parameters, we optimized the structures of H_2NO with zero, two, and four water molecules. Bond lengths and angles for structures optimized imposing C_s or C_{2v} symmetry are given in Table I. For the unsolvated radical, the C_{2v} structure corresponds to the planar transition state between two C_s minima. For the structures including water molecules, unconstrained optimizations lead to C_1 structures (see Sec. IV and Fig. 3). Although this analysis cannot replace a sampling of solvent configurations in a dynamic simulation of the solution, some first trends can be recognized. With an increasing number of water molecules, the N–O bond length increases slightly from 1.282 to 1.291 Å for the C_s structures, and a similar trend is found for the transition states. The N–H bond length does not change in a systematic way. An increase from 118.0° to

TABLE I. Optimized geometrical parameters (distances in angstrom, angles in degrees), isotropic hfcc a (MHz), as well as the g tensor for H_2NO , $\text{H}_2\text{NO} + 2\text{H}_2\text{O}$, and $\text{H}_2\text{NO} + 4\text{H}_2\text{O}$ molecules from unrestricted, scalar relativistic BP86/ZORA-QZ4P calculations (the g tensor was calculated, in a restricted, spin-orbit ZORA calculation). Additionally, inversion barriers $\Delta E(C_{2v} - C_s)$ (kJ/mol) are given. Experimental values are shown for comparison. The N–H bond length in Ref. 14 is an assumption to determine the other structural parameters. Note that the signs for the coupling constants have only been determined in the gas-phase study.

	H_2NO C_{2v}	H_2NO $\cdot 2\text{H}_2\text{O}$ C_{2v}	H_2NO $\cdot 4\text{H}_2\text{O}$ C_{2v}	H_2NO C_s	H_2NO $\cdot 2\text{H}_2\text{O}$ C_s	H_2NO $\cdot 4\text{H}_2\text{O}$ C_s	Exp.	
							water ^a	gas phase ^b
$r(\text{NO})$	1.281	1.282	1.290	1.282	1.285	1.291		1.280
$r(\text{NH})$	1.023	1.022	1.027	1.025	1.023	1.028		1.01
HNH	119.6	120.0	120.1	118.0	119.3	121.4		122.7
$\Delta E(C_{2v} - C_s)$	0.22	0.04	0.03					
θ	0.0	0.0	0.0	17.6	14.6	9.4		
$a(^{14}\text{N})$	10.0	11.5	13.1	17.8	16.8	13.6	35.9	27.10 ± 0.11
$a(\text{H})$	-36.5	-38.1	-39.2	-25.3	-30.8	-38.8	-35.9	-29.5 ± 0.20
g_{iso}	2.0088	2.0080	2.0080	2.0091	2.0082	2.0080	2.0057(1)	

^aReference 16.

^bReference 14.

TABLE II. Isotropic hfcc a (MHz) and g tensor for H_2NO , $\text{H}_2\text{NO}+2\text{H}_2\text{O}$, and $\text{H}_2\text{NO}+4\text{H}_2\text{O}$ from unrestricted, scalar relativistic BP86/ZORA-QZ4P calculations (the g tensor was calculated in a restricted, spin-orbit ZORA calculation). Water molecules in parenthesis denote calculations in which structures were taken from optimizations including the water molecules, while the water molecules have not been considered in the ESR calculations. For all structures, we give the out-of-plane bending angle θ (degrees).

	H_2NO C_s	H_2NO $\cdot 2\text{H}_2\text{O}$ C_s	H_2NO $\cdot (2\text{H}_2\text{O})$ C_s	H_2NO $\cdot 4\text{H}_2\text{O}$ C_s	H_2NO $\cdot (4\text{H}_2\text{O})$ C_s
θ	17.6	14.6	14.6	9.4	9.4
$a(^{14}\text{N})$	17.8	16.8	15.3	13.6	10.7
$a(\text{H})$	-25.3	-30.8	-28.7	-38.8	-35.7
g_{iso}	2.0091	2.0082	2.0091	2.0080	2.0090

119.3° and 121.4° can be observed for the H–N–H bond angle when adding two and four water molecules, respectively, for the C_s structures. For the structures with a planar H_2NO molecule, this increase is much smaller (from 119.6° to 120.1°).

With an increasing number of water molecules, the out-of-plane bending angle θ decreases for the minimum structures from 17.6 via 14.6 to only 9.4° for zero, two, and four explicit water molecules. Also the inversion barrier, estimated from the energy difference between the planar (C_{2v}) and pyramidal (C_s) structures, decreases from 0.22 (no water) to 0.03 kJ/mol (four water molecules), but in all cases, the barrier is almost zero. This will be discussed in some more detail in Sec. V. The corresponding hfcc's also show a systematic behavior for both nitrogen and hydrogen: $a(^{14}\text{N})$ decreases from 17.8 via 16.8 to 13.6 MHz and $a(\text{H})$ decreases from -25.3 via -30.8 to -38.8 with an increasing number of water molecules. Experimentally, the hfcc for hydrogen is larger (less negative, -29.5 MHz) *in vacuo* than in solution (-35.9), which is in line with the calculated microsolvation effects. But the hfcc for nitrogen is larger in water (35.9 MHz vs 27.1 MHz *in vacuo*), which is in disagreement with our findings for these small clusters.

It is instructive to separate the structural effect of the water molecules from their electronic effect. For this purpose, we calculated the ESR hyperfine couplings for the structures obtained from optimizations of $\text{H}_2\text{NO} \cdot 2\text{H}_2\text{O}$ and $\text{H}_2\text{NO} \cdot 4\text{H}_2\text{O}$, but omitted the water molecules in the calculation of the ESR parameters. The results are shown in Table II. As can be seen, the electronic effect of the water molecules is an *increase* of 1.5 MHz ($2\text{H}_2\text{O}$) and 2.9 MHz ($4\text{H}_2\text{O}$) for $a(^{14}\text{N})$, while the total decrease of this hfcc is caused by the structural change. For hydrogen, electronic and structural effects of the water molecules work in the same direction: changing the structure of H_2NO to that of the $\text{H}_2\text{NO} \cdot 2\text{H}_2\text{O}$ cluster decreases the hfcc from -25.3 to -28.7 MHz, and including the water molecules in the calculation leads to a further decrease to -30.8 MHz. Similarly, going to the $\text{H}_2\text{NO} \cdot 4\text{H}_2\text{O}$ structure changes $a(\text{H})$ from -25.3 to -35.7 MHz, and inclusion of the water molecules yields a value of -38.8 MHz. The structural effect apparently dominates for these small clusters.

Conclusions on the electronic effect of the water mol-

TABLE III. Isotropic hfcc a (MHz) for $\text{H}_2\text{NO} \cdot 2\text{H}_2\text{O}$ and $\text{H}_2\text{NO} \cdot 4\text{H}_2\text{O}$ from unrestricted, scalar relativistic BP86/ZORA-QZ4P supermolecule and frozen-density embedding calculations. All structures have been fully optimized without symmetry constraints. Water molecules in parenthesis denote calculations in which structures were taken from optimizations including the water molecules, while the water molecules have not been considered in the ESR calculations. For all structures, we give the out-of-plane bending angle θ (degrees).

	$\text{H}_2\text{NO} \cdot 2\text{H}_2\text{O}$	$\text{H}_2\text{NO} \cdot (2\text{H}_2\text{O})$	$\text{H}_2\text{NO} \cdot 4\text{H}_2\text{O}$	$\text{H}_2\text{NO} \cdot (4\text{H}_2\text{O})$
supermolecule				
θ	10.1	10.1	1.2	1.2
$a(^{14}\text{N})$	13.98	12.49	12.78	10.26
$a(\text{H})$	-34.73	-32.69	-38.75	-36.21
embedding in frozen $(\text{H}_2\text{O})_n$ clusters				
$a(^{14}\text{N})$	13.69		11.85	
$a(\text{H})$	-34.34		-38.69	
embedding in polarized frozen $(\text{H}_2\text{O})_n$ clusters				
$a(^{14}\text{N})$	13.97		12.32	
$a(\text{H})$	-34.75		-39.24	

ecules can also be drawn from the C_{2v} structures in Table I, for which there is no change of the angle θ . The structural effect due to the water molecules should thus be small. The hfcc for nitrogen increases (from 10.0 to 13.1 MHz) with an increasing number of water molecules, while the hfcc for hydrogen decreases (from -36.5 to -39.2 MHz).

We can conclude that structural and electronic effects in this microsolvation study work in the same direction for $a(\text{H})$, but obviously, they work in opposite directions for $a(^{14}\text{N})$. The average ESR parameters in solution and gas phase will depend critically on the distribution of the various possible structures, in particular, concerning the out-of-plane bending angle θ with its low-energy inversion barrier.

IV. VALIDATION OF THE SOLVENT MODEL

The validation of the frozen-density embedding as a solvent model involves (i) an assessment of its accuracy for short-range or microsolvation effects, and (ii) a test on the convergence of the hfcc's with the size of the solvent shell, to ensure a proper modeling of the bulk solvent effects.

Short-range solvation effects on the hfcc's of nitrogen and hydrogen, such as hydrogen bonding, are assessed by comparing supermolecule and frozen-density embedding calculations for small H_2NO -water clusters. Since only electronic effects are studied here, we reoptimized the structures of small clusters with two and four H_2O molecules without symmetry constraints. The structures from this unconstrained optimization, which are shown in Fig. 3, are 1.1 ($2\text{H}_2\text{O}$) and 4.4 ($4\text{H}_2\text{O}$) kJ/mol lower in energy than the corresponding C_s structures studied in Sec. VI.

In Table III results are shown for supermolecule and frozen-density calculations on these structures. All results are obtained from unrestricted, scalar relativistic ZORA calculations (BP86/ZORA-QZ4P). A fully converged self-consistent field (SCF) calculation is carried out to determine the densities of the embedding $(\text{H}_2\text{O})_2$ and $(\text{H}_2\text{O})_4$ clusters for the frozen-density calculations; simpler sum-of-molecular-

TABLE IV. Isotropic hfcc a (MHz) for $\text{H}_2\text{NO} + 2\text{H}_2\text{O}$ from unrestricted, scalar relativistic BP86/ZORA-QZ4P embedding calculations with different basis sets for the frozen system. Additionally, results are given for a sum-of-fragments calculation of the frozen density, in which LDA/ZORA-TZP has been used to generate the water fragments.

	QZ4P	TZP	DZP	DZ	LDA/TZP, sum-of-fragments
$a(^{14}\text{N})$	13.69	13.82	13.88	13.93	13.90
$a(\text{H})$	-34.34	-34.53	-34.60	-34.56	-34.62

densities superpositions are tested below. If a polarized frozen density is used, i.e., if one freeze-and-thaw cycle⁴⁹ is performed—in which the density of the water molecules is calculated in the presence of a frozen H_2NO radical density—the results for the $\text{H}_2\text{NO} \cdot 2\text{H}_2\text{O}$ cluster agree almost perfectly with the supermolecule calculations: The hfcc's for hydrogen and nitrogen are -34.75 and 13.97 MHz (polarized frozen-density embedding) compared to -34.73 and 13.98 MHz (supermolecule calculation). Further freeze-and-thaw cycles change the hfcc values by less than 0.02 MHz. If the water molecules are completely omitted for this structure, we obtain values of -32.69 and 12.49 MHz for $a(^1\text{H})$ and $a(^{14}\text{N})$, respectively. This effect is very similar to the one already observed for the C_s structures in Sec. III. As can be seen, already the nonpolarized frozen-density calculation yields most of the effect of the water molecules with hyperfine splittings of -34.34 (^1H) and 13.69 MHz (^{14}N). For the cluster with four water molecules, there is a slightly larger deviation between supermolecule and embedding calculations, but also here the embedding captures most of the effect of the water molecules. This can be expected, especially for the hydrogen hfcc, since the border between the frozen and nonfrozen regions is much closer to the hydrogen atoms for the $\text{H}_2\text{NO} \cdot (\text{H}_2\text{O})_4$ cluster than for the $\text{H}_2\text{NO} \cdot (\text{H}_2\text{O})_2$ cluster.

We would also like to note that spin polarization of the environment can, in principle, be modeled by the frozen-density embedding. This effect can be included by using freeze-and-thaw cycles in combination with spin-unrestricted frozen-density preparation calculations. By comparing freeze-and-thaw cycles with spin-restricted frozen densities for the water molecules to those with spin-unrestricted frozen solvent densities for a small H_2NO —water cluster, we found that the spin polarization of the solvent molecules is low, leading to changes in the hyperfine coupling constants which are smaller than those of the density relaxation (ca. 0.1–0.3 MHz).

In Table IV, we compare the results of frozen-density calculations with different basis sets for BP86/ZORA calculations. The inclusion of scalar-relativistic effects in the frozen density does not have a significant influence on the results. Nevertheless, we will use the ZORA approach also for the frozen system for internal consistency with the embedded system. We observe that the basis set effect for the *frozen density* is relatively small with variations of 0.13–0.26 MHz compared to the largest basis set.

While frozen densities from fully converged BP86 calculations have been used in the above tests, such calculations

are quite inefficient and can suffer from convergence problems for very large $(\text{H}_2\text{O})_n$ clusters. The construction of the density for systems with large solvent shells would be the time-limiting step in the calculation if a conventional SCF procedure was used. Subsequent statistical analyses of several hundreds of snapshots would be computationally very demanding. However, for smaller water shells than used here, calculations with fully converged solute-solvent clusters have been presented.⁵⁰ In Ref. 22, it has been shown that the simpler LDA can be used for the frozen part, and that it is advantageous to calculate the frozen density from a superposition of molecular densities. In this case, the size of the solvation shell is in principle unlimited, since its density is obtained as a sum of densities of individual water molecules. The calculation on n water molecules (scaling with n^3 in conventional KS-DFT calculations) is thus replaced by n calculations on single water molecules (scaling with n^1). Furthermore, especially the outer solvation shells can—to a good approximation²²—be represented by rigid water molecules (all in the same structure). In this way, the density of the whole frozen system is obtained by performing m calculations on the nearest m solvent molecules in their original structures from the CPMD simulation, while only one additional calculation on the standard rigid water model is necessary to obtain the density for all other $n-m$ outer water molecules. This leads to an n^0 scaling for the construction of the molecular fragment densities, plus a (very rapid) superposition step, in which the density for the rigid model is copied to the positions of all outer water molecules, and in which all fragment densities are added. We tested this method for the small $\text{H}_2\text{NO} \cdot 2\text{H}_2\text{O}$ cluster (see Table IV). As might be expected for these weakly interacting water molecules, the effect of the sum-of-fragment approach in combination with the simple LDA has only a minor effect on the hfcc: $a(^1\text{H})$ changes by 0.08 MHz (from 13.82 to 13.90 MHz), and $a(^{14}\text{N})$ by 0.09 MHz (from -34.53 to -34.62 MHz) for the TZP basis set. A more extensive test on the effect of this sum-of-fragment approximation on the results of frozen-density calculations can be found in Ref. 22.

In order to check the convergence of the hyperfine splittings with respect to the solvation shell, we took an arbitrary snapshot from a CPMD simulation (see Sec. V) and created (nonperiodic) substructures from that (periodic) structure with different numbers of solvent molecules. The hyperfine splittings a for hydrogen and nitrogen (^{14}N) were calculated for the H_2NO radical with a water shell of between 0 and 100 water molecules. The largest cluster is shown in Fig. 4.

Here we used individual fragment densities for the innermost 20 water molecules, while an optimized H_2O structure (BP86/TZP) was used as a rigid model for the outer water molecules. LDA/ZORA-TZP calculations within the sum-of-fragment approach have been used to generate the frozen densities. The resulting isotropic hyperfine coupling constants a are shown in Fig. 5. For both H and ^{14}N it can be seen that the largest effect is due to the first solvation shell, i.e., from the nearest ten water molecules. For 30 and more water molecules, only slight variations in the values for a are observed. For the statistical analysis presented in Sec. V, we

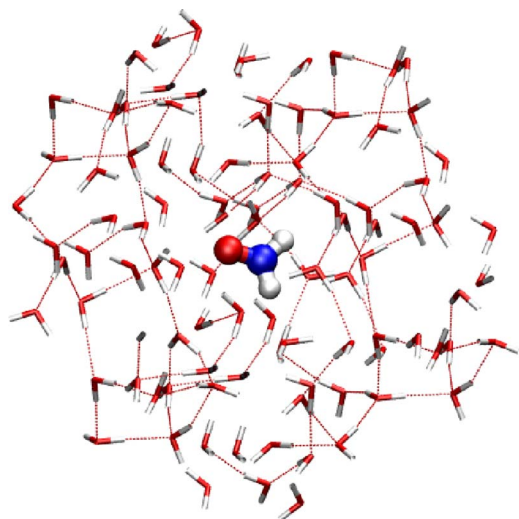


FIG. 4. Structure of an arbitrary snapshot from a CPMD simulation of H_2NO in water, including the nearest 100 water molecules. The convergence of the hyperfine splitting constants in the QM/QM frozen-density embedding was tested for substructures of this cluster.

take the 75 water molecules closest to the radical into consideration for every snapshot from the CPMD simulation in aqueous solution.

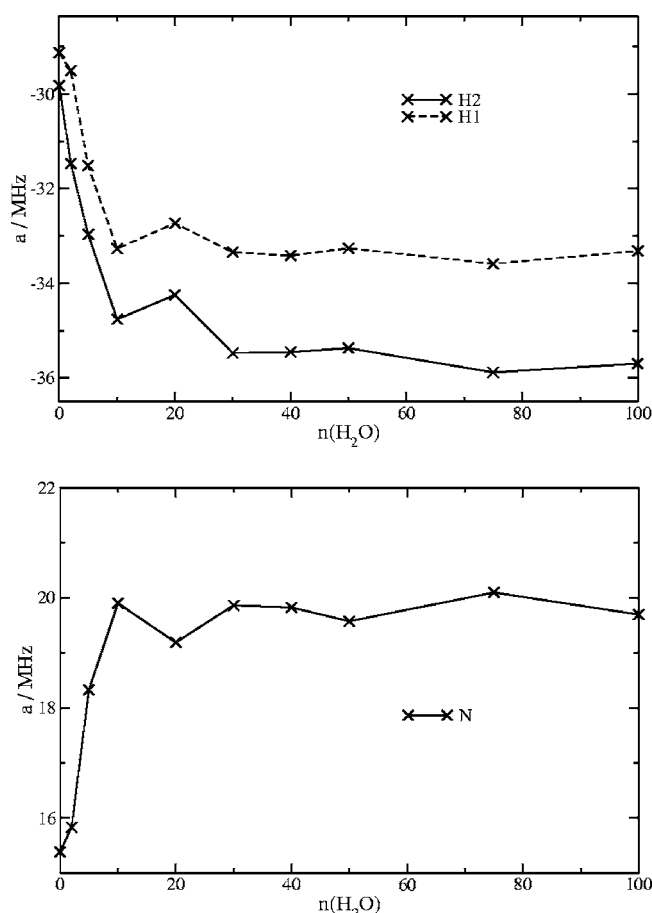


FIG. 5. Convergence of the isotropic hyperfine coupling constants a for H (top) and ^{14}N (bottom) as a function of the number of water molecules in the solvent shell. Note that the two hydrogen atoms are not equivalent in this snapshot.

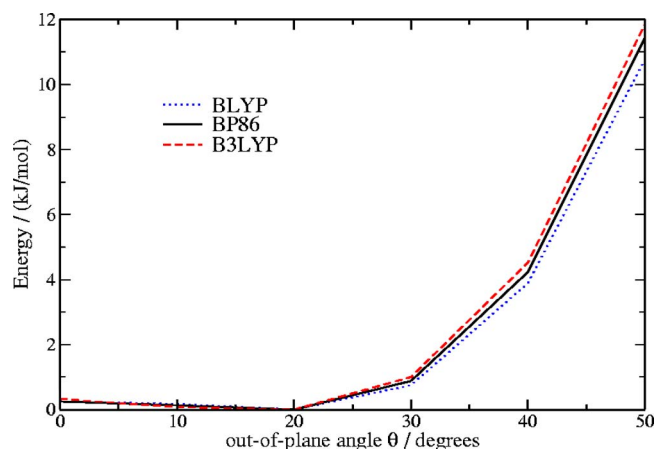


FIG. 6. Potential-energy variation along the out-of-plane bending angle θ . All other internal coordinates have been optimized (BP86/ZORA-QZ4P). For comparison, results are shown for BP86, BLYP, and B3LYP (post-SCF energy calculations using BP86/ZORA-QZ4P orbitals). All energies are given in units of kJ/mol with respect to the structure with $\theta=20^\circ$.

V. STATISTICAL ANALYSIS OF CPMD AND MC SNAPSHOTS

A statistical analysis of the ESR parameters has been performed for snapshots from a first-principles-based Monte Carlo (MC) simulation for the gas phase and a CPMD simulation for the aqueous solution. For the gas phase, we combined the results of two independent MC simulations to get a larger number of configurations. Two effects must be considered and accurately be described in these calculations in order to produce a reliable solvent shift for the hyperfine coupling constants. First, the electronic effect of the solvent at a given solute structure must be taken into account, and second, the effect of the solvent on the probability distribution of structural parameters. Since it is known that other radicals, such as OH, can form hemibonded structures (i.e., structures with an oxygen-oxygen interaction forming a three-electron bond) in water,⁵¹ which appears to be overemphasized by the standard DFT functionals, we took a particular look at this effect for H_2NO also. However, no such hemibond is formed for this radical, since the orbital energy of the unpaired electron is too high. Otherwise, such a structure could have a significant impact on the ESR parameters.

As mentioned before, the most important structural parameter in our case is the out-of-plane bending angle θ . The probability distribution for this angle naturally depends on the potential-energy curve along this internal coordinate. We calculated the potential energies along this angle using BP86/ZORA-QZ4P, where all other internal coordinates were optimized for a given out-of-plane angle. The results are shown in Fig. 6, where we also give energies calculated (post-SCF) with the BLYP and B3LYP functionals as an internal consistency check. The lowest-energy structure in this scan with steps of 10° is obtained for $\theta=20^\circ$ (the angle for the fully optimized structure is 17.6° , see Table I). The inversion barriers are very low with 0.2(BP86) to 0.3(BLYP, B3LYP) kJ/mol, and they are in good agreement with the B3LYP and UQCISD[T] data from Ref. 43. The corresponding minimum-energy out-of-plane angles found there are 16.90° (UQCISD[T]) and 16.6° (B3LYP), which are—in view of the

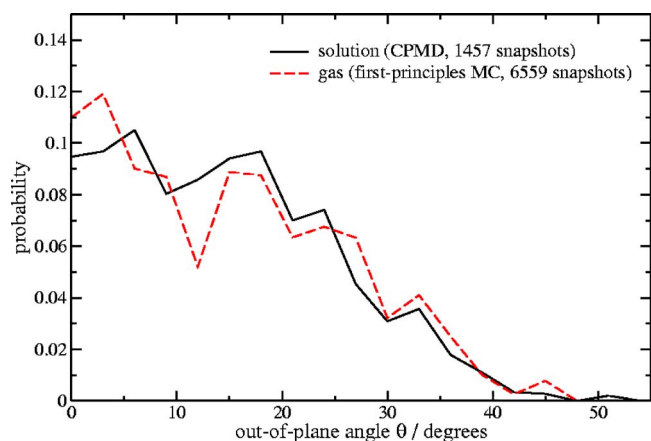


FIG. 7. Probability of finding a particular out-of-plane bending angle θ in the CPMD simulation of the H_2NO radical. The results shown are based on 1457 and 6559 snapshots for the trajectories in solution (solid line) and in the “gas phase” (isolated molecule; dashed line). The probabilities are given in intervals of 3° , i.e., in units of $1/(3^\circ)$.

very shallow potential-energy surface—in good agreement with our structure. Experimentally, there is some evidence for the planarity of the H_2NO radical, but it has been suggested that this is due to a double-minimum potential for the out-of-plane vibration with a very low barrier.¹⁴ This is in perfect agreement with the KS-DFT and UQCISD[T] results.

Also for the energies, we observe strong discrepancies between the results presented above and the ROHF results from Ref. 18. ROHF leads to a minimum-energy structure with $\theta=36.5^\circ$ and an inversion barrier of 3.6 kJ/mol, while the energy increase for angles $>40^\circ$ is less steep than in our calculation. Obviously, the probability distribution resulting from the ROHF energy profile along θ cannot be considered reliable. This is important to note, since the probability distribution has a large impact on the averaged hyperfine coupling constants.

From all structures generated in the simulations, we determined the probabilities of finding particular out-of-plane bending angles θ . The results are shown in Fig. 7. Both probability distributions are still rather noisy, but it can be recognized without doubt that the distributions in the gas phase and solution are quite similar. The maxima in the probability distributions occur at small angles (close to planarity), and the distributions are quite broad up to angles of about 25° – 30° . Angles larger than 40° are not very probable. This confirms the energy profile in Fig. 6. The average out-of-plane bending angle is 16.8° in the gas phase, and 16.7° in solution. The difference in the average angles is thus much smaller than the standard error in the average angle (1.7° for the gas phase). This is in contrast with the classical Monte Carlo study in Ref. 18 (average angle in the gas phase: 30.7° ; in solution: 19.9°), which used a force field fitted to ROHF energies. The potential-energy minimum in that case corresponds to a much too large θ angle of 36.5° . It was suggested in Ref. 18 that the inversion barrier almost completely vanishes in solution, which is in agreement with our study. But in our calculation, the barrier is also very small in the gas phase.

From the above-mentioned sets of structures, we calcu-

TABLE V. Isotropic hfcc a (MHz) for structures from a *first-principles*-based MC (gas) or CPMD (solution) simulation, averaged over 1311 (gas) or 200 (solution) configurations. Besides the average values, we also give the maxima of the hfcc distributions as shown in Fig. 8. The values for the optimized isolated structures of C_{2v} and C_s symmetry are included for comparison. Additionally, experimental values and results from a continuum solvation model are shown. Note that the signs of the hyperfine coupling constants are not determined in Ref. 16. They have been inferred from the study in Ref. 14 and from our calculations.

	$a(^{14}\text{N})$	$a(\text{H})$
Optimized molecule		
C_{2v}	10.0	−36.5
C_s	17.8	−25.3
gas-phase simulation (1311 conf.)		
average	19.8	−22.6
max.	10.5	−36.5
exp. ^a	27.10	−29.51
simulation aqueous solution (200 conf.)		
average	21.6	−28.5
max.	14.5	−38.5
exp. ^b	35.9	−35.9
shift		
average	1.8	−5.9
max.	4.0	−2.0
B3LYP/PCM/EPR-3 ^c	0.6	−10.6
exp. ^{a, b}	8.8	−6.4

^aReference 14.

^bReference 16.

^cReference 43.

lated hyperfine coupling constants for every fifth structure of the first 1000 structures in solution and of the 6559 structures obtained from the MC simulation. Using every structure for the hfcc calculation would not add new significant information, since subsequent structures, especially in the MC simulation, often show a considerable correlation. This means that 200 snapshots have been calculated in solution, while 1311 snapshots have been considered for the gas phase. We used the frozen-density embedding approach as described above to model the effect of the water molecules in these calculations. The average values and the maxima of the distributions are shown in Table V. The probabilities for different values of the hfcc are shown in Fig. 8 for the gas phase and for aqueous solution. These plots now show the combined effect of the structural and electronic changes of the hyperfine coupling constants. First, it can be seen that the maximum positions of the probabilities shift as expected from the experimental values: For $a(^{14}\text{N})$, the maximum shifts by 4.0 MHz from 10.5 (gas) to 14.5 MHz (water), and for $a(^1\text{H})$, it shifts by −2.0 MHz from −36.5 (gas) to −38.5 MHz (water). The shifts in the average values of the hyperfine coupling constants are qualitatively the same, but they differ in magnitude. The average of $a(^{14}\text{N})$ shifts by +1.8 from 19.8 MHz (gas) to 21.6 MHz (water), and the average of $a(^1\text{H})$ shifts by −5.9 from −22.6 to −28.5. The experimental shifts are 8.8 (^{14}N) and −6.4 MHz (^1H) if the values from the microwave study in Ref. 14 are used for the gas phase. Also the results of 30.3 MHz (^{14}N) and −33.1 MHz (^1H) from Ref. 15 are

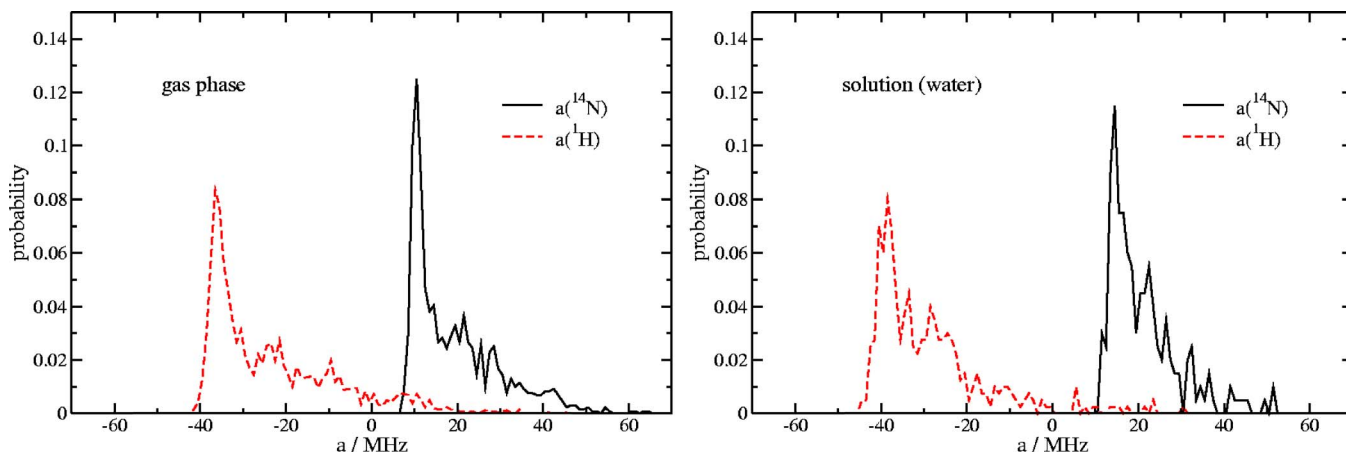


FIG. 8. Distribution of the isotropic hyperfine coupling constants a from 1311 snapshots of a *first-principles*-based Monte Carlo simulation of H_2NO in the gas phase (left) and from 200 snapshots of a CPMD simulation of H_2NO in water (right). Probabilities are given for intervals of 1 MHz.

sometimes assumed as “gas-phase” values, and in combination with the results for aqueous solution from Ref. 16 they would yield solvents shift of 5.6 (^{14}N) and -2.8 MHz (^1H). These values, however, were obtained in a xenon matrix at a much lower temperature (77 K) than used in our simulation, and a rather strong temperature dependence of the hfcc’s for H_2NO *in vacuo* was found in Ref. 19. We note that the B3LYP/polarizable continuum model (PCM) study in Ref. 43 has even larger problems with the shift for nitrogen (0.6 MHz), and overestimates the (absolute value of the) shift for hydrogen (-10.6 MHz).

As can be seen from Fig. 8, there is no large change in the distribution of the hyperfine coupling constants in the gas phase and solution (although we could see a change towards smaller angles for the optimized clusters in Sec. III, and corresponding changes in the hyperfine splittings). In the gas phase, the distributions look slightly broader than in solution, but the effect is not large in view of the noise still present for this rather small number of snapshots (the classical MC simulation in Ref. 18 used 2×10^6 steps for the averaging).

To investigate the electronic effect of the solvent at a given angle θ in gas phase and solution, we plot the hfcc’s

observed in our simulations as a function of θ in Fig. 9 (only every 20th snapshot has been used for the gas-phase simulation in that plot for clarity of presentation). Also shown are quadratic fits to these curves, the coefficients of which are collected in Table VI. As can be seen, the quadratic coefficients for a given nucleus are rather similar, so that the fitted curves run almost parallel. Only for larger angles ($\theta > 20^\circ$) in the case of nitrogen this is no longer well fulfilled. The offsets in the fitted curves for small angles ($\theta \approx 0$) are 4.1 MHz for ^{14}N (solution minus gas), and -3.4 MHz for ^1H , and these values can be regarded as estimates for the average electronic effect of the solvent. The results are in qualitative agreement with the experimental shifts, which again demonstrates that structural effects—although important for the average hyperfine coupling constant—are similar in gas phase and solution.

We would also like to note the similarities between the gas-phase curve in Fig. 9 and the one obtained for partially optimized structures in Fig. 2, which demonstrates that the out-of-plane bending angle has, among all structural parameters of this radical, by far the most important effect on the hfcc.

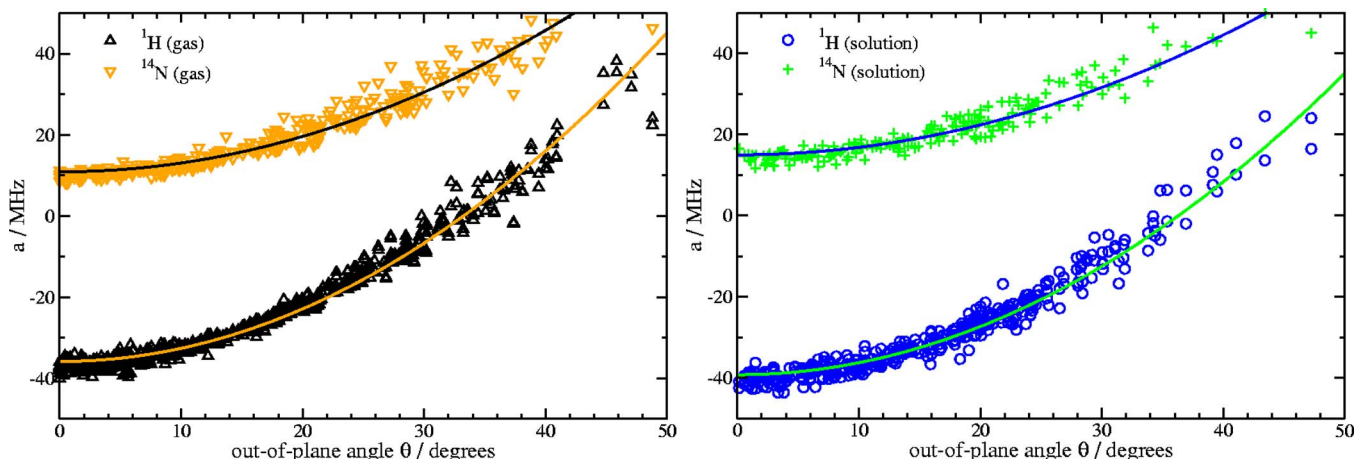


FIG. 9. Isotropic hfcc a for ^1H and ^{14}N for H_2NO in the gas phase (left) and in aqueous solution (right) as a function of the out-of-plane bending angle θ . Shown are data points for every 20th snapshot in the gas-phase simulation (327 in total) and for every fifth of the first 1000 snapshots in solution (200 in total) for clarity of presentation (note that there are two data points for each snapshot in case of ^1H because of the two nonequivalent hydrogen atoms). Also given are the quadratic fits to these data sets.

TABLE VI. Coefficients for the fits $a(\theta) = a_0 + a_1\theta^2$ of the isotropic hfcc a as a function of the out-of-plane bending angle θ . The values were obtained by fitting the data sets shown in Fig. 9.

	a_0/MHz	$a_1/(\text{MHz}/\text{deg}^2)$
^{14}N (gas)	10.860	0.0218
^{14}N (solution)	14.935	0.0185
^1H (gas)	-39.218	0.0297
^1H (solution)	-35.831	0.0324

VI. DISCUSSION AND CONCLUSION

In this study, we could show that the frozen-density embedding can be used to reliably model solvent effects on ESR hyperfine coupling constants in connection with an appropriate way to sample the configurational space in gas phase and solution.

The comparisons of embedding and supermolecule calculations for small H_2NO —water clusters demonstrate that specific effects due to hydrogen bonding are reproduced by the embedding scheme. In principle, it also allows to describe spin polarization effects in the environment, although they are of minor importance in the present example. This is a clear advantage over QM/molecular mechanics (MM) or continuum solvation models, which additionally rely on empirical information for the solvent. Due to the efficiency of the embedding approach, it is straightforward to choose the size of the explicitly considered solvent shell as large as necessary to converge the hyperfine coupling constants. In the present example, it allowed us to perform a statistical analysis of 200 snapshots with 75 explicit water molecules.

The microsolvation study reveals that for small $\text{H}_2\text{NO} \cdot n\text{H}_2\text{O}$ clusters increasing numbers of water molecules lead to smaller out-of-plane angles θ , which causes a decrease in the hfcc's for both nitrogen and hydrogen. The electronic effect of the water molecules works in the same direction for ^1H , but in the opposite direction for ^{14}N .

This indicates that a sophisticated treatment for both structural and electronic effects of macrosolvation is necessary in order to reproduce the experimental trends, in particular for nitrogen, to assess which of the two effects will be stronger in solution. For an aqueous solution, this was achieved by a CPMD simulation. Special care has to be taken in the calculation of average gas-phase reference values. On the one hand, standard thermostats in (CP)MD simulations fail in the present case of a very small molecule, since the exchange of energy between different degrees of freedom is extremely slow. But on the other hand, the small number of degrees of freedom allowed us to perform a *first-principles*-based Monte Carlo simulation, which ensures a proper sampling of the accessible configurational space of the molecule.

The trend in these simulations shows some similarities to the microsolvation study. The average out-of-plane angle θ is slightly smaller in solution than in the gas phase. The strong dependence of the hfcc's on θ suggests that there should be a small change towards smaller values for both $a(^1\text{H})$ and $a(^{14}\text{N})$. The pure electronic effect can be estimated from the shift between the data sets for gas phase and solution in Fig.

9. In a first approximation (for small angles, which have the highest probability), the curve of $a(^1\text{H})$ is shifted by ≈ -3 MHz in solution, and the curve of $a(^{14}\text{N})$ is shifted by $\approx +4$ MHz.

To calculate the change in the average hfcc's upon solvation, we also have to consider the changes in the probability for different structures, in particular, for different out-of-plane angles. In contrast with the classical Monte Carlo simulation in Ref. 18, we do not find a significant difference in the probability distribution of the out-of-plane bending angle between gas phase and solution. We attribute the differences in Ref. 18 to the ROHF-based potential-energy surface with a minimum at a much too large angle θ . The total shifts in the average hfcc in our study are -5.9 MHz (^1H) and $+1.8$ MHz (^{14}N), compared to -6.4 and $+8.8$ MHz, respectively, in experiment. From these calculated shifts we can—by subtracting the estimates for the electronic contribution—give rough estimates for the structural contributions of ≈ -3 MHz for hydrogen and ≈ -2 MHz for nitrogen.

Like in the microsolvation study, we see that structural and electronic effects cause shifts in opposite directions for nitrogen. But in the solution study the electronic effects dominate, so that the calculated shift for ^{14}N is too low, but it still has the same direction (plus sign) as in experiment. The quantitative modeling is complicated by the fact that already slight changes in the probability distribution have large effects on the average hyperfine coupling constants. Although the electronic effect might still be underestimated a bit by neglecting relaxation and spin-polarization effects in the frozen density, our tests showed that the (combined) errors introduced by these approximations should not be larger than ≈ 1 MHz. To arrive at full quantitative agreement with experiment, structural differences between gas phase and solution would probably have to be modeled even more accurately (i.e., by using more sophisticated electronic structure methods in combination with large statistical test sets of snapshots). Further calculations of ESR properties with frozen-density embedding will be necessary to fully clarify this point. The results for hydrogen on the other hand are very encouraging and agree with the experimental shift within 0.5 MHz, although they might partially benefit from error cancellation in structural and electronic effects.

The frozen-density embedding thus turns out to be a powerful and promising tool for the calculation of shifts in ESR hyperfine coupling constants also for larger molecules in solution or radicals in more complex environments.

ACKNOWLEDGMENT

We thank Professor Michiel Sprik for helpful discussions about proper sampling of the gas-phase structures. One of the authors (J.N.) gratefully acknowledges funding by a Forschungstipendium from the Deutsche Forschungsgemeinschaft (DFG). Another author (M.J.L.) acknowledges a grant from the Dutch National Research School Combination “Catalysis by Design” (NRSC-C). Another author (P.B.) acknowledges the CNR-ISTM (Consiglio Nazionale delle Ricerche—Istituto di Scienze e Tecnologie Molecolari) for

funding. One of the authors (T.A.W.) was supported by the Swiss National Science Foundation and the Federal Office for Education and Science acting as the Swiss COST office.

- ¹M. Kaupp, M. Bühl, and V. G. Malkin, *Calculation of NMR and EPR Parameters* (Wiley-VCH, Weinheim, 2004).
- ²M. Munzarová and M. Kaupp, J. Phys. Chem. A **103**, 9966 (1999).
- ³P. Belanzoni, E. van Lenthe, and E. J. Baerends, J. Chem. Phys. **114**, 4421 (2001).
- ⁴L. Hermosilla, P. Calle, J. M. García de la Vega, and C. Sieiro, J. Phys. Chem. A **109**, 1114 (2005).
- ⁵R. Improta and V. Barone, Chem. Rev. (Washington, D.C.) **104**, 1231 (2004).
- ⁶D. M. Chipman, J. Phys. Chem. A **104**, 11816 (2000).
- ⁷E. Langella, R. Improta, and V. Barone, J. Phys. Chem. A **124**, 11531 (2002).
- ⁸M. Kaupp, C. Remeyi, J. Vaara, O. L. Malkina, and V. G. Malkin, J. Am. Chem. Soc. **124**, 2709 (2002).
- ⁹N. Rega, M. Cossi, and V. Barone, J. Chem. Phys. **105**, 11060 (1996).
- ¹⁰I. Ciofini, R. Reviakine, A. Arbuznikov, and M. Kaupp, Theor. Chem. Acc. **111**, 132 (2004).
- ¹¹V. Barone, A. Bencini, M. Cossi, A. D. Matteo, M. Mattesini, and F. Totti, J. Am. Chem. Soc. **120**, 7069 (1998).
- ¹²T. Yagi and O. Kikuchi, J. Phys. Chem. A **103**, 9132 (1999).
- ¹³M. Pavone, C. Benzi, F. D. Angelis, and V. Barone, Chem. Phys. Lett. **395**, 120 (2004).
- ¹⁴H. Mikami, S. Saito, and S. Yamamoto, J. Chem. Phys. **94**, 3415 (1991).
- ¹⁵M. Jinguji, T. Imamura, H. Murai, and K. Obi, Chem. Phys. Lett. **84**, 335 (1981).
- ¹⁶O. P. Chawla and R. W. Fessenden, J. Phys. Chem. **79**, 2693 (1975).
- ¹⁷J. Q. Adams, S. W. Nicksic, and J. R. Thomas, J. Chem. Phys. **45**, 654 (1966).
- ¹⁸H. Takase and O. Kikuchi, J. Phys. Chem. **98**, 5160 (1994).
- ¹⁹V. Barone, A. Grand, C. Minichino, and R. Subra, J. Phys. Chem. **97**, 6355 (1993).
- ²⁰T. A. Wesolowski and A. Warshel, J. Phys. Chem. **97**, 8050 (1993).
- ²¹T. A. Wesolowski, J. Am. Chem. Soc. **126**, 11444 (2004).
- ²²J. Neugebauer, M. J. Louwerse, E. J. Baerends, and T. A. Wesolowski, J. Chem. Phys. **122**, 094115 (2005).
- ²³J. Neugebauer, C. R. Jacob, T. A. Wesolowski, and E. J. Baerends, J. Phys. Chem. A **109**, 7805 (2005).
- ²⁴P. Cortona, Phys. Rev. B **44**, 8454 (1991).
- ²⁵J. P. Perdew, in *Electronic Structure of Solids*, edited by P. Ziesche and H. Eschrig (Akademie Verlag, Berlin, 1991), p. 11.
- ²⁶A. Lembarki and H. Chermette, Phys. Rev. A **50**, 5328 (1994).
- ²⁷T. A. Wesolowski, H. Chermette, and J. Weber, J. Chem. Phys. **105**, 9182 (1996).
- ²⁸T. A. Wesolowski, J. Chem. Phys. **106**, 8516 (1997).
- ²⁹Amsterdam density-functional program, Theoretical Chemistry, Vrije Universiteit, Amsterdam, URL: <http://www.scm.com>.
- ³⁰G. te Velde, F. M. Bickelhaupt, E. J. Baerends, C. Fonseca Guerra, S. J. A. van Gisbergen, J. G. Snijders, and T. Ziegler, J. Comput. Chem. **22**, 931 (2001).
- ³¹A. D. Becke, Phys. Rev. A **38**, 3098 (1988).
- ³²J. P. Perdew, Phys. Rev. B **33**, 8822 (1986).
- ³³E. van Lenthe, E. J. Baerends, and J. G. Snijders, J. Chem. Phys. **99**, 4597 (1993).
- ³⁴E. van Lenthe, E. J. Baerends, and J. G. Snijders, J. Chem. Phys. **101**, 9783 (1994).
- ³⁵E. van Lenthe, J. G. Snijders, and E. J. Baerends, J. Chem. Phys. **105**, 6505 (1996).
- ³⁶E. van Lenthe, P. Wormer, and A. van der Avoird, J. Chem. Phys. **107**, 2488 (1997).
- ³⁷E. van Lenthe, A. van der Avoird, and P. Wormer, J. Chem. Phys. **108**, 4783 (1998).
- ³⁸P. E. Blöchl, Phys. Rev. B **50**, 17953 (1994).
- ³⁹C. Lee, W. Yang, and R. G. Parr, Phys. Rev. B **37**, 785 (1988).
- ⁴⁰G. Kresse and D. Joubert, Phys. Rev. B **59**, 1758 (1999).
- ⁴¹D. Frenkel and B. Smit, *Understanding Molecular Simulation* (Academic, New York, 2002).
- ⁴²M. P. Allen and D. J. Tildesley, *Computer Simulation of Liquids* (Oxford University Press, Oxford, 1989).
- ⁴³V. Barone, Chem. Phys. Lett. **262**, 201 (1996).
- ⁴⁴A. D. Becke, J. Chem. Phys. **98**, 5648 (1993).
- ⁴⁵P. J. Stephens, F. J. Devlin, C. F. Chabalowski, and M. J. Frisch, J. Phys. Chem. **98**, 11623 (1994).
- ⁴⁶B. Engels, in *Calculation of NMR and EPR Parameters*, edited by M. Kaupp, M. Bühl, and V. G. Malkin (Wiley-VCH, Weinheim, 2004), pp. 438–492.
- ⁴⁷T. Nakano, K. Morihashi, and O. Kikuchi, Chem. Phys. Lett. **186**, 572 (1991).
- ⁴⁸K. Morihashi, H. Takase, and O. Kikuchi, Bull. Chem. Soc. Jpn. **63**, 2113 (1990).
- ⁴⁹T. A. Wesolowski and J. Weber, Int. J. Quantum Chem. **61**, 303 (1997).
- ⁵⁰J. R. Asher, N. L. Doltsinis, and M. Kaupp, J. Am. Chem. Soc. **126**, 9854 (2004).
- ⁵¹P. Vassilev, M. J. Louwerse, and E. J. Baerends, Chem. Phys. Lett. **398**, 212 (2004).